nature geoscience

SUPPLEMENTARY INFORMATION

DOI: 10.1038/NGEO2623

Himalayan megathrust geometry and relation to topography revealed by the Gorkha earthquake

J. R. Elliott, R. Jolivet, P. J. González, J.-P. Avouac, J. Hollingsworth, M. P. Searle and V. L. Stevens

1 Optical Offsets

To determine the co-seismic horizontal displacement field due to the Gorkha earthquake, we use optical image correlation to measure the displacement of pixels between pre- and post-earthquake satellite images. We are able to resolve sub-pixel displacements of less than 1/15th of the Landsat8 pixel resolution (i.e. < 1 m) using the COSI-Corr software package[1–4], which is available for free download from www.tectonics.caltech.edu/slip_history/spot_coseis/index.html. Landsat8 imagery is ideally suited to this method, for several reasons: (1) images are acquired regularly, with repeat global coverage every 16 days, (2) image footprints are large (120 x 120 km), thereby covering the entire region of surface deformation in few acquisitions, (3) the nadir (i.e. vertical) look angle of Landsat8 results in similar viewing geometries between images, which helps to increase the signal-to-noise ratio, (4) the deformation field is resolved perpendicular to the look angle (i.e. the horizontal plane for nadir images), thereby providing measurements complementary to InSAR (which is sensitive to vertical displacements), (5) the nadir look angle is insensitive to topographic residuals produced during orthorectification of the satellite images (such residuals are produced when a lower resolution digital elevation model, DEM, is used during the orthorectification process), and (5) Landsat8 images are freely available from the USGS as an orthorectified product - see[5] for additional details.

Landsat8 images are typically acquired at 10am each morning. Consequently, the illumination characteristics (i.e. shadows) vary in every image acquired throughout the year according to the position of the sun. Because shadows produce sharp edges in satellite images, they strongly influence the correlation. Therefore, to reduce the effect of differing shadows biasing the displacement field, we correlate Landsat8 images acquired at a similar time of year, thereby yielding images with similar illumination characteristics (i.e. sun azimuth and elevation). In addition to having similar illumination characteristics, we also require images with minimal cloud cover. From the Landsat8 archive, we found two suitable images from the (pre-earthquake) 13th May 2014 (sun azimuth: 109°, sun elevation: 68°,), and (post-earthquake) 1st June 2015 (az.: 100°,

Table 1 | Details of interferograms for the M_w 7.8 25^{th} April 2015 Gorkha Earthquake and largest aftershock. Columns show Sentinel-1/ALOS-2 tracks, satellite directions, incidence angles (°), dates of acquisition, time interval ΔT, and post-seismic interval ΔPT. The number of data points used for the slip inversion are also given.

Satellite	Track #	Direction asc/dsc	Incidence °	Master yyyymmdd	Slave yyyymmdd	ΔT dys	ΔPT dys	Data pts
Gorkha Mw 7.8 Mainshock 25th April 2015								
SEN-1	019	dsc	34–44	20150417	20150429	12	4	360
SEN-1	085	asc	34–44	20150409	20150503	24	8	476
SEN-1	121	dsc	34–44	20150424	20150506	12	11	433
ALOS-2	048	dsc	18–43	20150222	20150503	70	8	582
ALOS-2	157	asc	33	20150221	20150502	70	7	262
Gorkha Mw 7.3 Aftershock 12th May 2015								
SEN-1	085	asc	34–44	20150503	20150515	12	3	576
SEN-1	121	dsc	34–44	20150506	20150518	12	6	654
ALOS-2	048	dsc	18–43	20150503	20150517	14	5	354

el.: 69°,). Band 8 (15 m resolution, panchromatic band) of both pre- and post- images was correlated using a multi-scale sliding window varying between 64 pixels and 32 pixels in dimension. Patches with the largest window size were correlated first, and if the correlation succeeded, smaller patches (decreasing by power of two) were correlated, while accounting for the previously found displacement. The process was iterated until the minimum window size was reached, or until the correlation failed, in which case the measurement found from the previous larger size was kept and the process moved on to the next area (see the COSI-Corr user manual, available with download of the COSI-Corr software). Displacement measurements were made horizontally and vertically every 8 pixels, resulting in correlation map of 120 m resolution. Additional noise was removed from the resulting EW and NS displacement maps by stripping out unlikely values. Due to a slight overlap of the charge coupled device (CCD) arrays on the Landsat8 sensor, the correlations contain a striping artefact, which was removed by stacking and subtracting the average artefact signal from the correlations; this was done using the destriping tool in COSI-Corr with a manual rotation of -13.6°. Linear detrending was performed to remove any ramps in the displacement map resulting from mis-registration of the input Landsat8 images. Finally, because the fault did not break the surface, the deformation field is dominated by a long-wavelength signal. To enhance this signal, we further suppress noise in the correlation results by applying a Non-Local Means filter (NLM parameters: noise parameter, 5; search area, 41 pixels; weighting method, linear regression), followed by a 3x3 median filter. Visual inspection of the filtered and raw correlation data together suggests the filtering has little or no influence on the wavelength of the displacement signal.

Our correlation results show a clear long-wavelength shortening signal in the north-south component, consistent with slip occurring at depth on the Main Himalayan Thrust. As with the SAR azimuth offsets, the noise in the data places little constraint on the inversion for the MHT geometry and they are therefore not used in the inversion, but comparison with the predicted north-south motion is shown in Supplementary Fig. 3.

Table 2 Full moment tensors from seismology and InSAR. The six components of the moment tensor (M_{rr}, M_{tt}, M_{pp}, M_{rt}, M_{rp}, M_{tp}) and the total moment M_0 are given. We calculate the percentage double-couple component DC of the InSAR and seismological solutions following the definition[6] where a pure double couple source (with eigenvalues λ of -1, 0, 1) is 100% and a compensated linear vector dipole (e.g. λ = -1/2, -1/2, 1) is 0%. $DC = 100 * \{1 - [(3 * |\lambda_2|)/(|\lambda_1| + |\lambda_3|)]\}$.

Source	Lon. °	Lat. °	Depth km	M_{rr} 10^{20}Nm	M_{tt} 10^{20}Nm	M_{pp} 10^{20}Nm	M_{rt} 10^{20}Nm	M_{rp} 10^{20}Nm	M_{tp} 10^{20}Nm	M_0 10^{20}Nm	DC %
Gorkha Mw 7.8 Mainshock 25th April 2015											
InSAR	85.3763	27.9104	14.2	2.0548	-1.8790	-0.17579	4.8682	-1.435	0.5758	5.48	100
GCMT	85.37	27.77	12	1.730	-1.790	0.056	7.520	-0.587	0.454	7.76	98
USGSMwc	85.1917	28.1972	10	1.9222	-1.9398	0.1760	5.0371	-0.5202	0.5607	5.45	92
Gorkha Mw 7.3 Aftershock 12th May 2015											
InSAR	86.1367	27.7505	14.3	0.1838	-0.1663	-0.0176	0.4338	-0.1410	0.0540	0.492	100
GCMT	86.10	27.56	12	0.2640	-0.2540	-0.0098	0.8520	-0.0440	0.1210	0.900	99
USGSMww	85.96	27.44	15.5	0.2657	-0.2635	-0.0220	0.9249	-0.1947	0.1179	0.989	98

References

[1] Leprince, S., Barbot, S., Ayoub, F. & Avouac, J. Automatic and Precise Orthorectification, Coregistration, and Subpixel Correlation of Satellite Images, Application to Ground Deformation Measurements. *IEEE Trans. Geosci. Remote Sens.* **45**, 1529–1558 (2007).

[2] Leprince, S., Ayoub, F., Klinger, Y. & Avouac, J.-P. Co-registration of optically sensed images and correlation (COSI-Corr): An operational methodology for ground deformation measurements. In *Geoscience and Remote Sensing Symposium, 2007. IGARSS 2007. IEEE International*, 1943–1946 (IEEE, 2007).

[3] Leprince, S., Muse, P. & Avouac, J. In-Flight CCD Distortion Calibration for Pushbroom Satellites Based on Subpixel Correlation. *IEEE Trans. Geosci. Remote Sens.* **46**, 2675–2683 (2008).

[4] Ayoub, F., Leprince, S. & Avouac, J.-P. Co-registration and correlation of aerial photographs for ground deformation measurements. *ISPRS Journal of Photogrammetry and Remote Sensing* **64**, 551–560 (2009).

[5] Zinke, R., Hollingsworth, J. & Dolan, J. F. Surface slip and off-fault deformation patterns in the 2013 M_W 7.7 Balochistan, Pakistan earthquake: Implications for controls on the distribution of near-surface coseismic slip. *G*^{3} **15**, 5034–5050 (2014).

[6] Jackson, J., Priestley, K., Allen, M. & Berberian, M. Active tectonics of the South Caspian Basin. *GJI* **148**, 214–245 (2002).

[7] Bilham, R., Bodin, P. & Jackson, M. Entertaining a great earthquake in Western Nepal: Historic inactivity and geodetic tests for the present state of strain. *Journal of Nepal Geological Society* **11**, 73–78 (1995).

[8] Ambraseys, N. N. & Douglas, J. Magnitude calibration of north Indian earthquakes. *GJI* **159**, 165–206 (2004).

[9] Martin, S. & Szeliga, W. A Catalog of Felt Intensity Data for 570 Earthquakes in India from 1636 to

2009. *Bull. Seismol. Soc. Am.* **100**, 562–569 (2010).

[10] Lindsey, E. *et al.* Line of Sight Displacement from ALOS-2 Interferometry: Mw 7.8 Gorkha Earthquake and Mw 7.3 Aftershock. *GRL* (2015).

[11] Galetzka, J. *et al.* Slip pulse and resonance of the Kathmandu basin during the 2015 Gorkha earthquake, Nepal. *Science* **349**, 1091–1095 (2015).

[12] Jackson, M. & Bilham, R. Constraints on Himalayan deformation inferred from vertical velocity fields in Nepal and Tibet. *JGR* **99**, 13897–13912 (1994).

[13] Ader, T. *et al.* Convergence rate across the Nepal Himalaya and interseismic coupling on the Main Himalayan Thrust: Implications for seismic hazard. *JGR* **117**, B04403 (2012).

[14] Stevens, V. & Avouac, J.-P. Coupling on the Main Himalayan Thrust. *GRL* **42**, 5828–5837 (2015).

[1]COMET, Department of Earth Sciences, University of Oxford, Oxford, OX1 3AN, UK, [2]COMET, Bullard Laboratories, Department of Earth Sciences, University of Cambridge, Cambridge, CB3 OEZ, UK, [3]COMET, School of Earth & Environment, University of Leeds, Leeds, LS2 9JT, UK, [4]Geological and Planetary sciences, California Institute of Technology, Pasadena, California, USA. [5]ARUP 13 Fitzroy Street, London, W1T 4BQ, UK, [6]Department of Earth Sciences, University of Oxford, Oxford, OX1 3AN, UK. *e-mail: john.elliott@earth.ox.ac.uk.

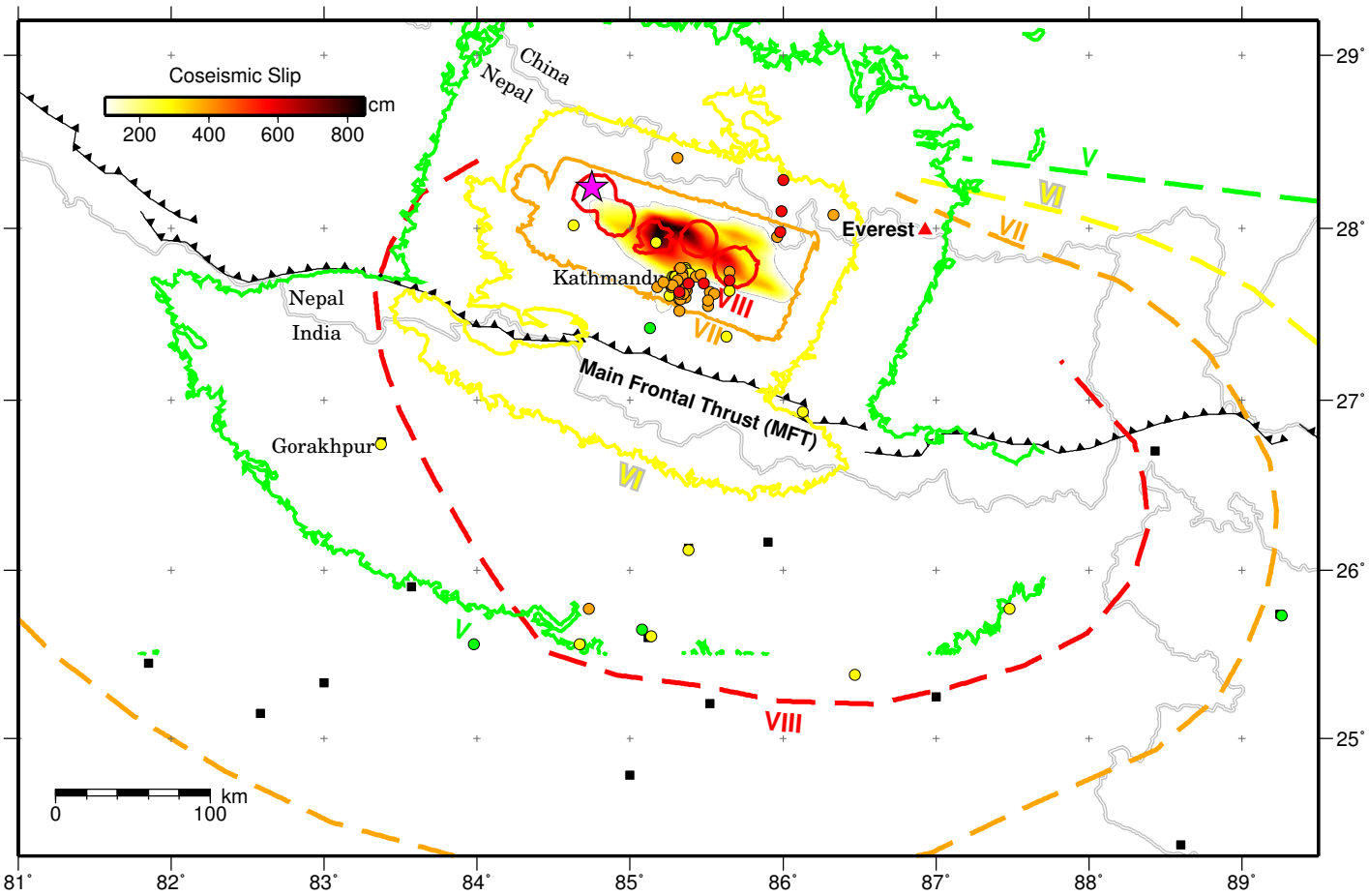

Supplementary Figure 1 | Shaking intensity comparison between the 2015 Gorkha earthquake and the 1833 earthquake. Comparison of the shaking on the Modified Mercalli Intensity scale estimated from the 1833 earthquake[7] (dashed coloured lines), compared to the synthetic shaking intensity as modelled for the Gorkha 2015 earthquake by the USGS (solid lines). It should be noted that the 1833 isoseismals were reinterpreted by[8] and have been superseded by the European Macroseismic Scale (EMS-98) intensity scale and we therefore overlay these EMS intensity values (coloured circles) from[9] as well. The highest USGS intensity values around Kathmandu are likely to be over predicted by more than 1 intensity scale (Bilham, pers comm). The mainshock slip distribution from this study is also shown, and has a similar rupture extent as that used by the USGS in modelling their estimate of the ground shaking.

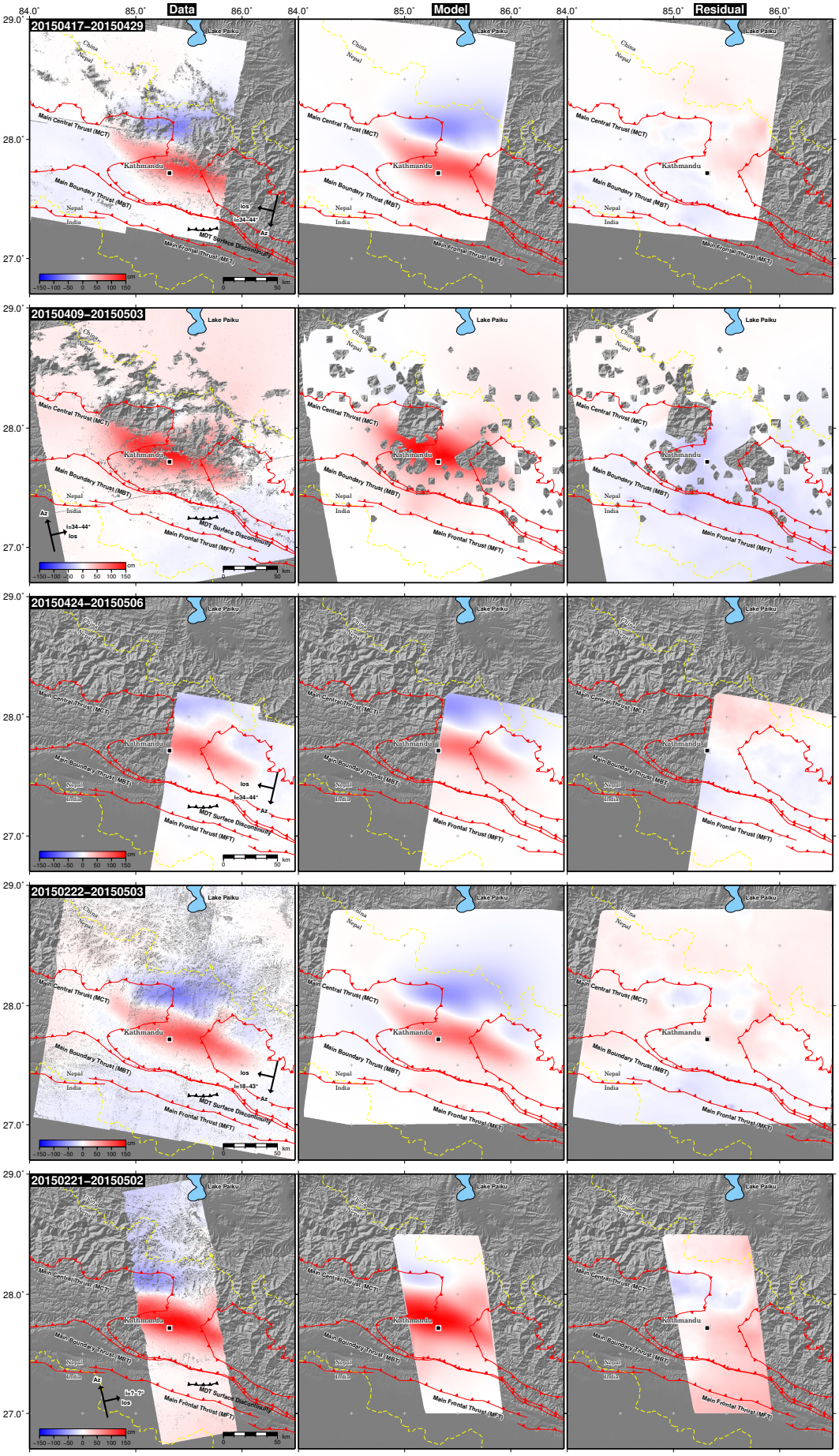

Supplementary Figure 2 | Fit of the predicted surface displacements to the InSAR data based upon the MHT geometry model. Data (left column), model (middle) and residuals (right) for the InSAR phase datasets from Sentinel-1 (first three rows) and ALOS-2[10] (last two rows) on ascending and descending tracks used in the constraining the MHT geometry. The satellite azimuth and look direction are denoted by the black arrows. Red lines with teeth are the surface trace of the Main Frontal/Boundary/Central Thrusts (MFT/MBT/MCT). The grey background is SRTM hillshaded topography.

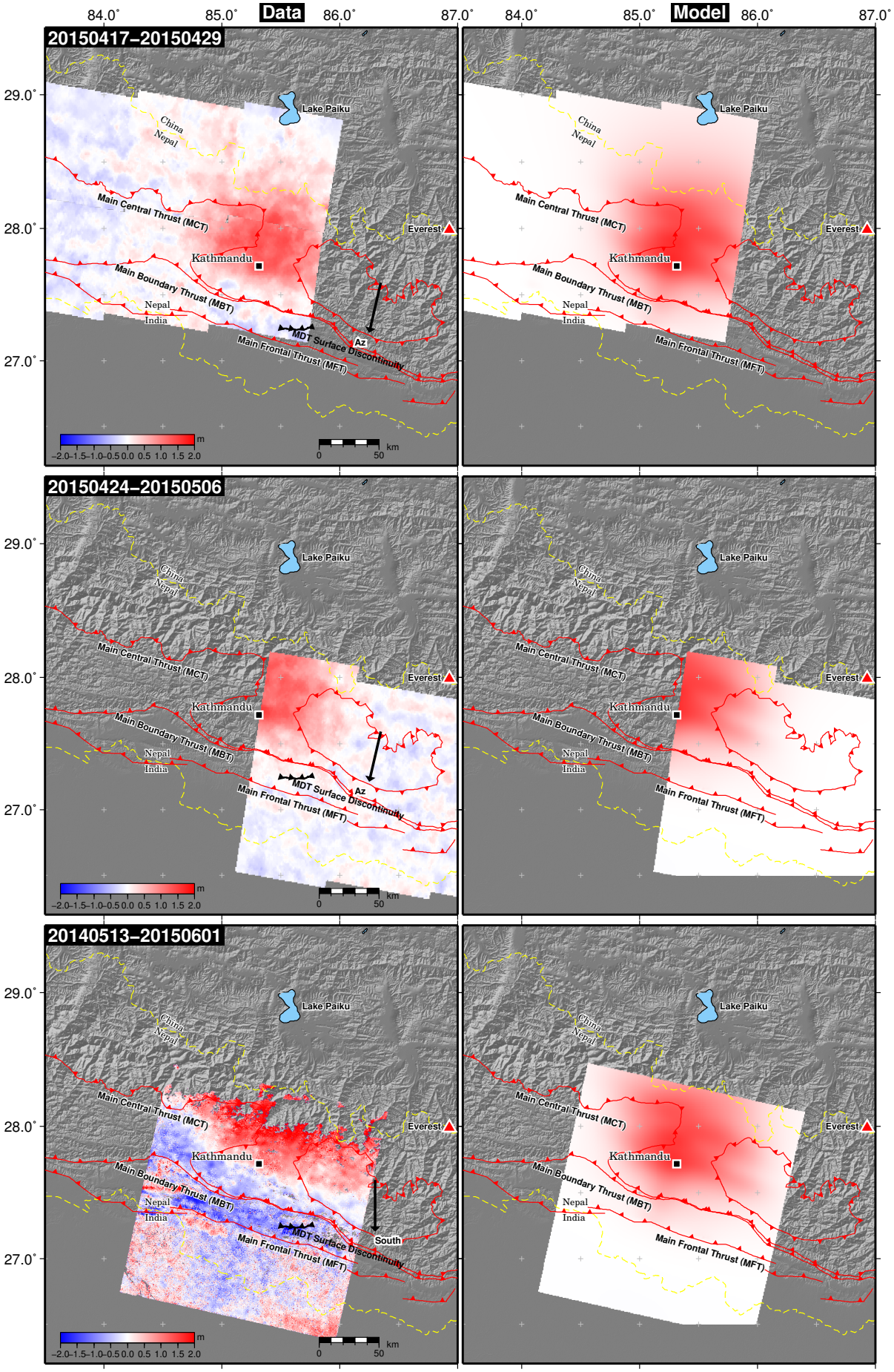

Supplementary Figure 3 | SAR and optical offset data with predicted model for comparison. Data and forward model for the offset datasets from Sentinel-1 azimuth amplitude correlation (top two rows) and the north-south component of Landsat8 correlation (bottom row). The black arrows indicate the measured offset direction. Red lines with teeth are the surface trace of the Main Frontal/Boundary/Central Thrusts (MFT/MBT/MCT). Due to the level of noise in the offset data, these datasets were not used to formally constrain the fault geometry nor slip model.

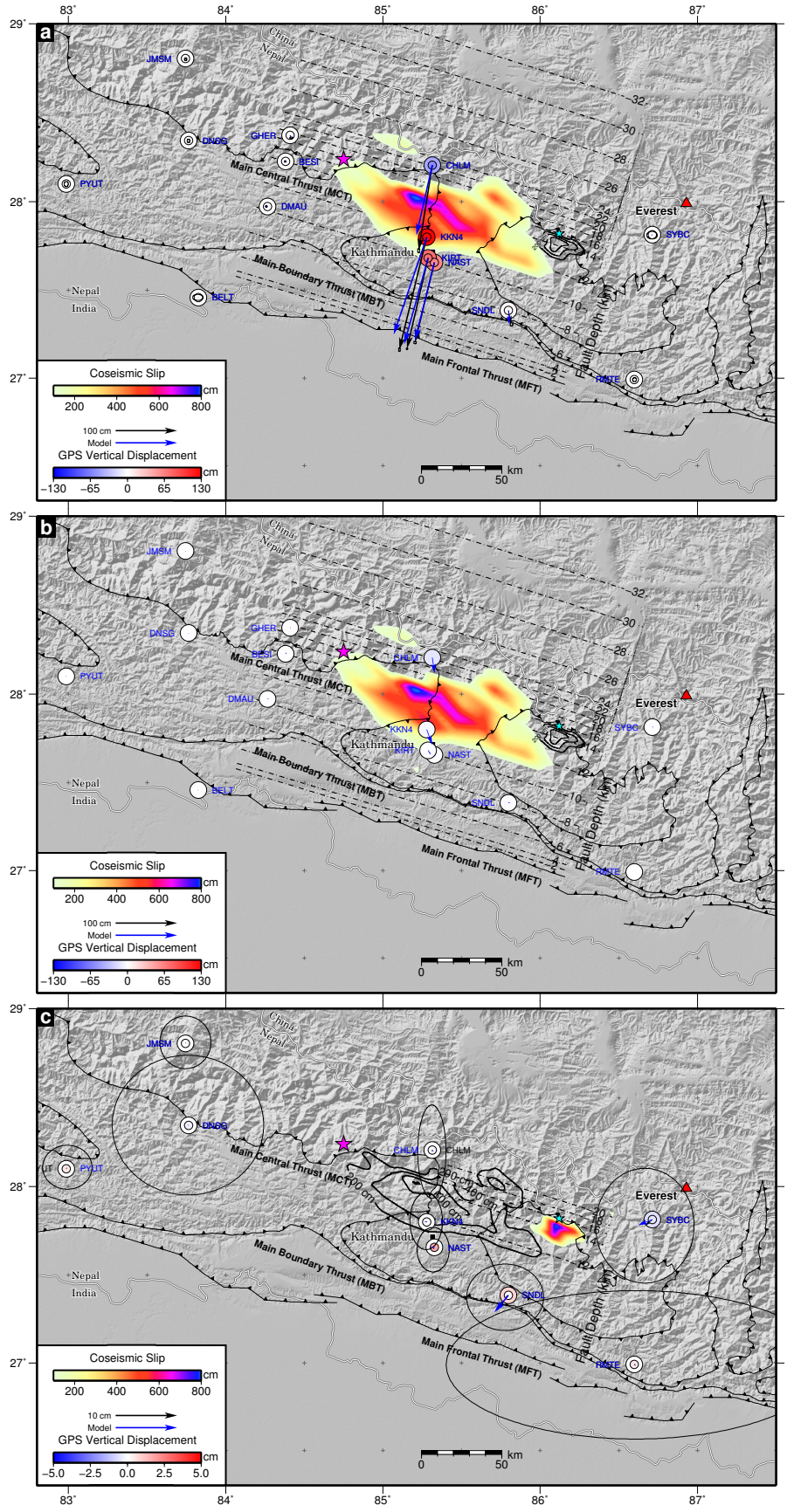

Supplementary Figure 4 | Fit to the GPS data. (a) GPS data[11] (black arrows) and model (blue arrows) for the mainshock horizontal displacements. Vertical displacements are denoted by blue-to-red coloured circles (inner=data, outer=model), and black ellipses denote 2-sigma errors. The coseismic slip distribution is also shown. The black contours indicate the slip due to the Mw 7.3 aftershock on the 12th May. The black dashed contours are depth to MHT in the model. (b) Residual misfit between the GPS data and model for both horizontal (arrows) and vertical (circles) displacements given at the same scale as in (a). (c) GPS displacement data for the 12th May Mw 7.3 aftershock (note the change in scale from the above plots). None of the GPS data show offsets measurable within error (black ellipses). The coseismic slip distribution for the aftershock based upon the InSAR data is also shown. The black contours indicate the slip due to the Mw 7.8 mainshock on the 25th April.

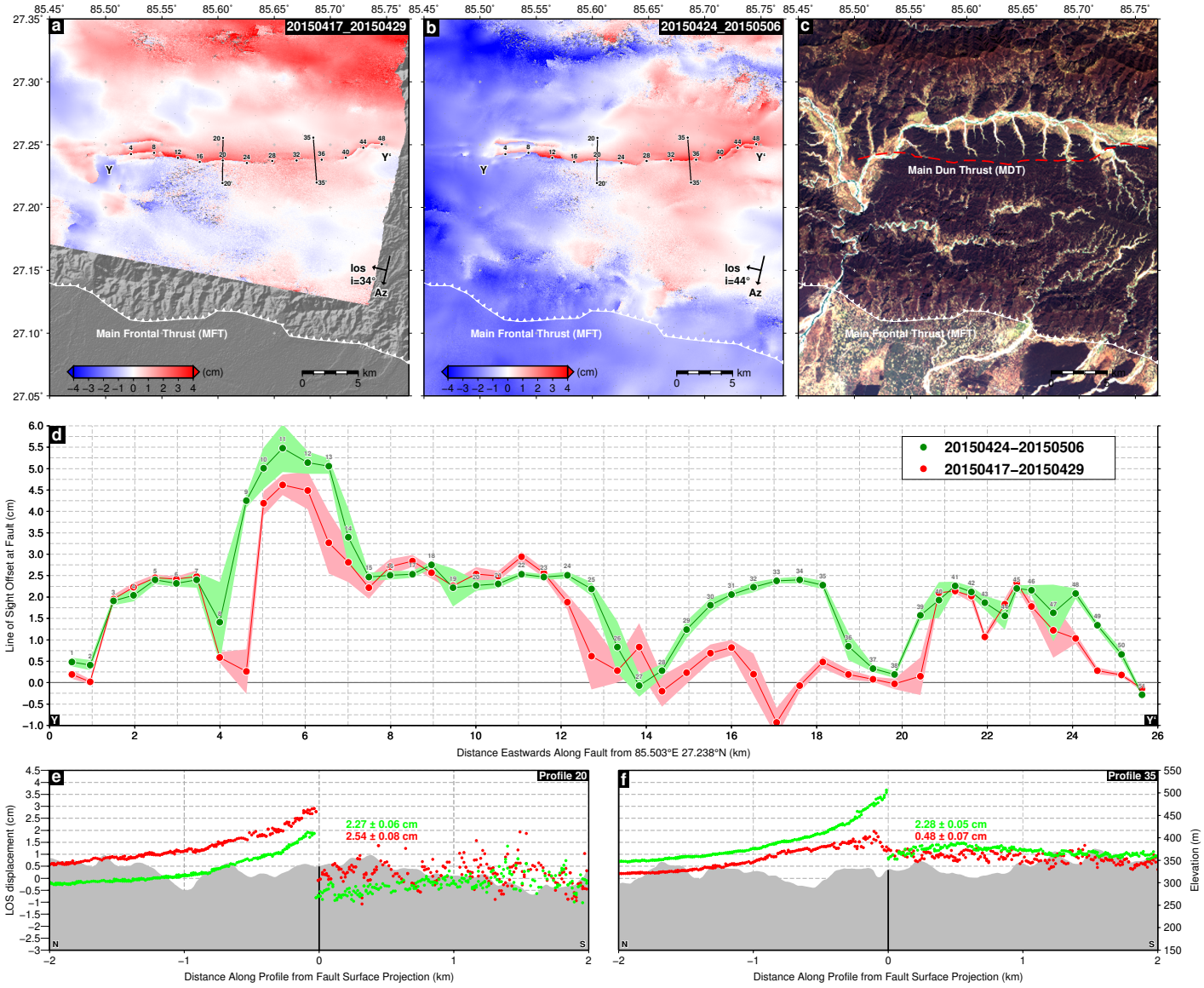

Supplementary Figure 5 | Surface offset imaged by InSAR along the Main Dun Thrust (MDT). (a) Sentinel-1 interferogram for the period 20150417–20150429 showing a 26 km long discontinuity in the measured deformation field. The interferogram covers a postseismic period of 4 days as well as the coseismic period. (b) Sentinel-1 interferogram for the period 20150424–201504506 covering 11 days of postseismic deformation, exhibiting the same surface displacement, with an additional break at the surface in the centre. (c) Landsat image of the area with the location of the surface discontinuity marked by the dashed red line. (d) Along fault profile (Y–Y') of the magnitude of the line-of-sight offsets at the surface taken from the difference in displacement measured from profiles perpendicular to the fault 25–125 m away from the surface trace every 500 m along strike (14 m size pixels). (e) Fault perpendicular profile number 20 (location shown in (a/b)) through the two interferograms (coloured dots) overlaid on SRTM topography (grey). (f) as for panel (e) except for profile number 35.

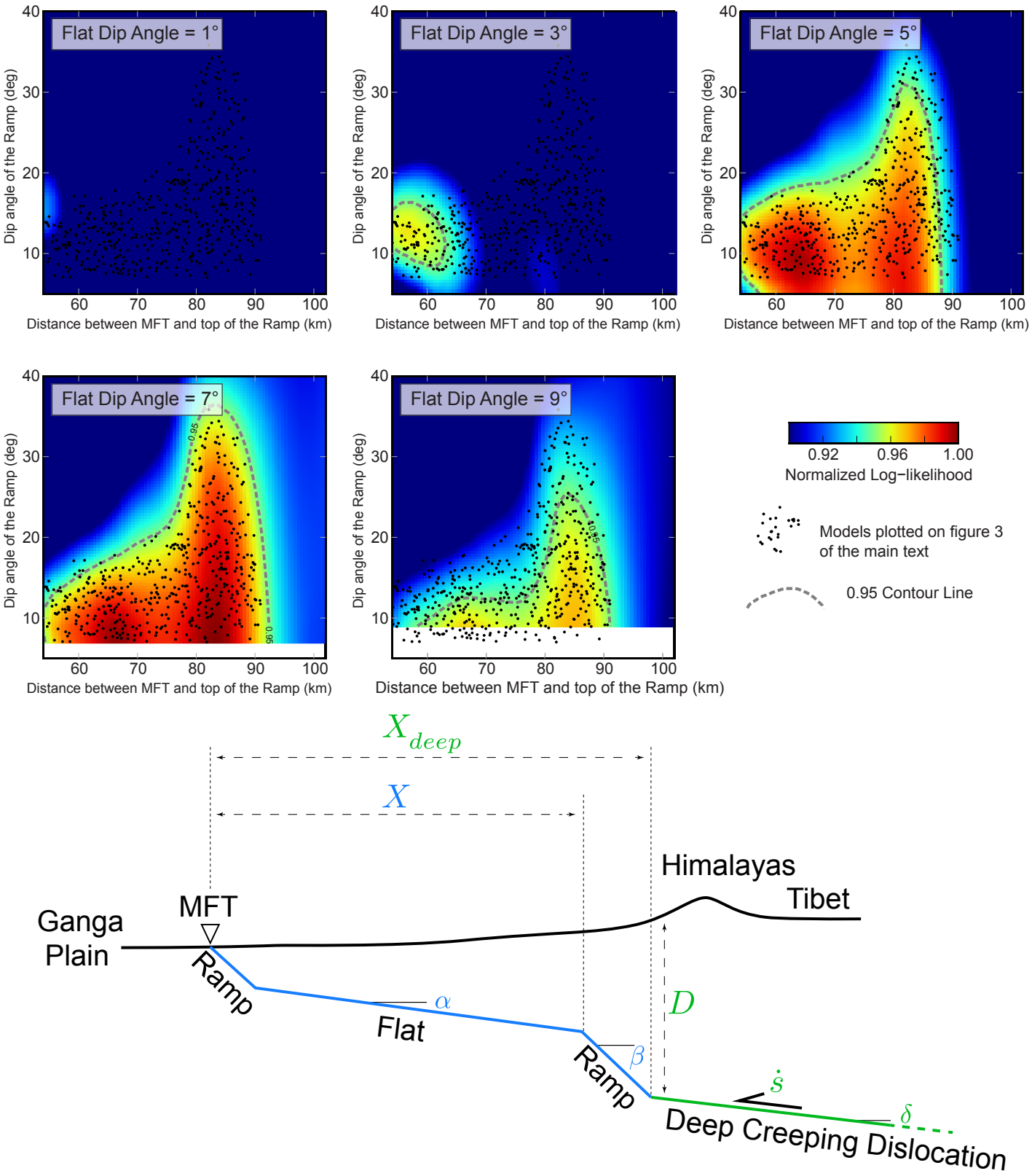

Supplementary Figure 6 | Log-Likelihood function of the geometrical parameters and schematic cross-section. Model log-likelihood for different values α of the dip angle of the flat portion of the MHT as a function of the dip angle of the mid-crustal ramp, β and the distance between the top of the ramp and the MFT, X. Gray dashed line is the 95% contour line. Black dots are 500 models randomly picked inside the 95% contour line. (bottom) Schematic cross-section across the Himalayan ranges to illustrate the geometrical parameters tested in our exploration of the possible geometries of the Main Himalayan Thrust (highlighted in blue) and for the exploration of the position of the deep creeping dislocation to model interseismic displacement rates (highlighted in green).

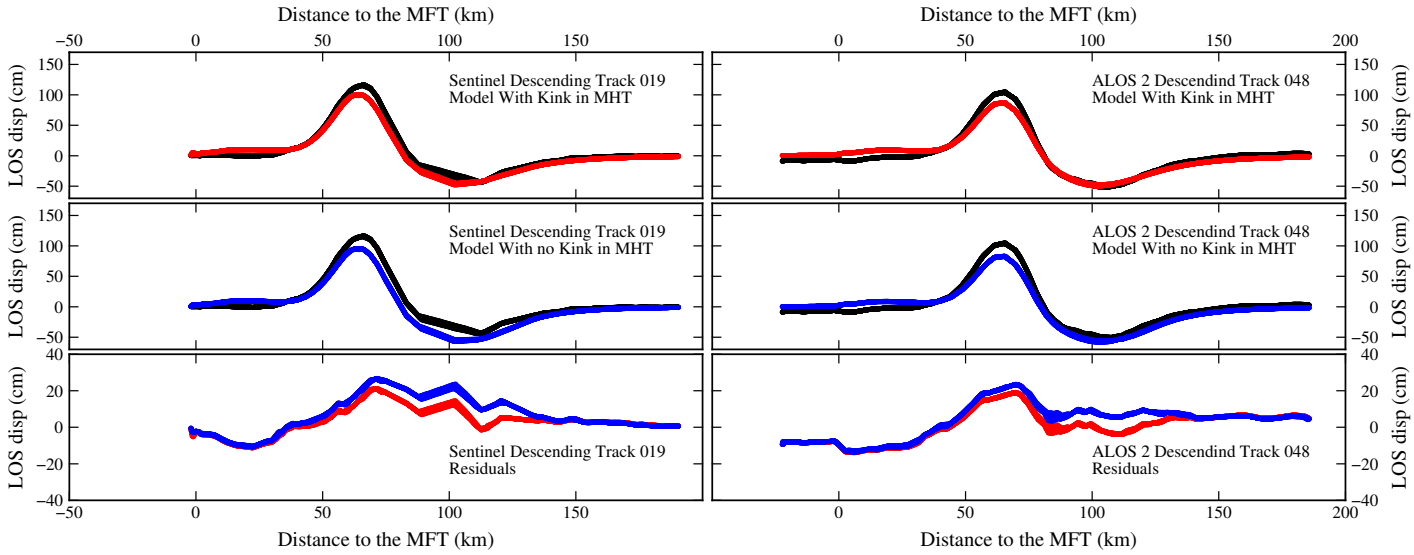

Supplementary Figure 7 Comparison of model predictions with and without a steep, mid-crustal, ramp along the MHT | MHT perpendicular profiles of Line-Of-Sight displacements for the Sentinel interferogram on descending track 19 (left) and ALOS interferogram on descending track 48 (right) for a model including a steep (20°), mid-crustal, ramp (top, in red) and without a mid-crustal ramp (center, in blue). Black dots are the measured LOS displacements. Lower row shows the residuals for the model with a ramp (red) and without a ramp (blue).

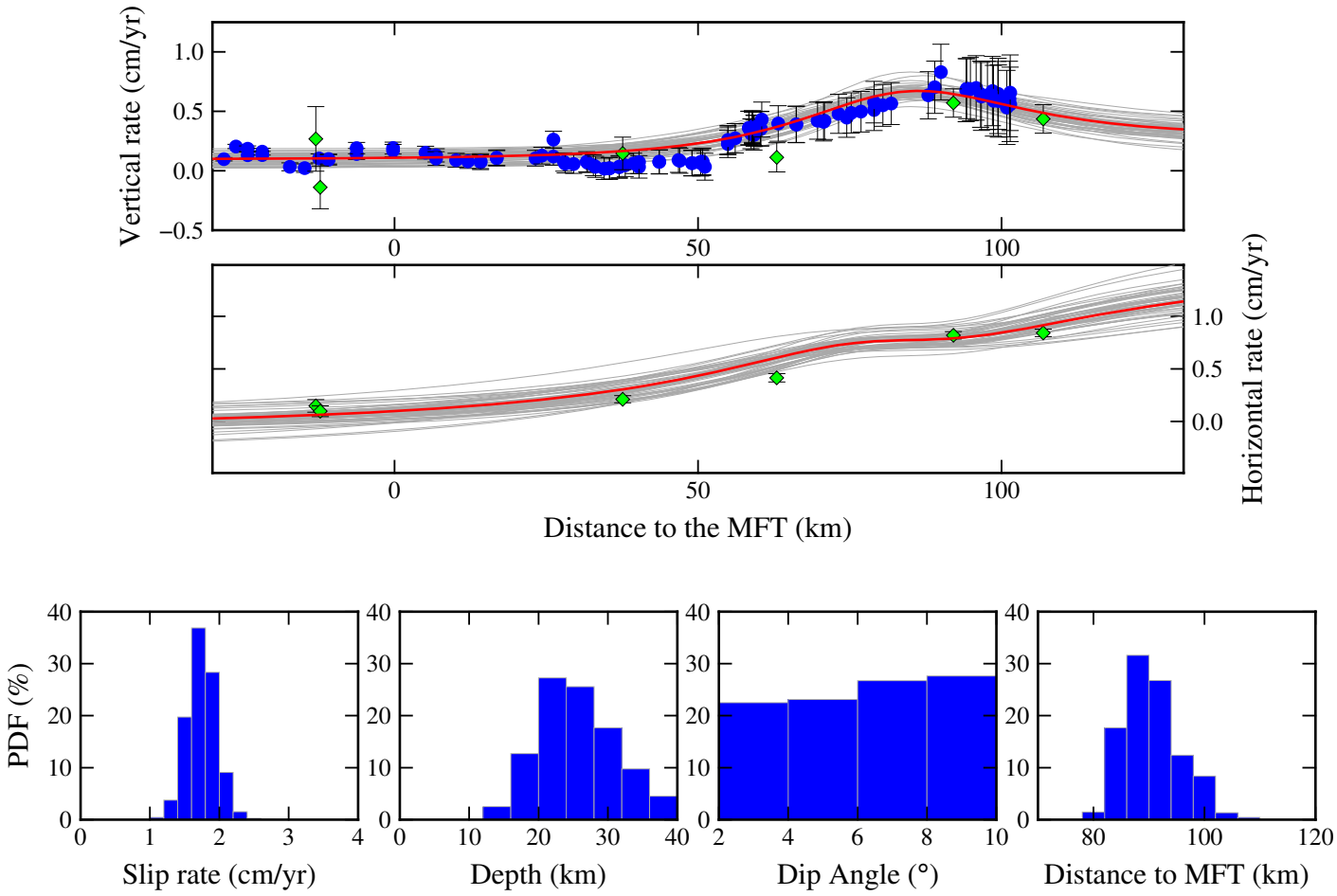

Supplementary Figure 8 | Exploration of parameters of the interseismic strain accumulation model. Vertical and horizontal displacement rates derived from levelling measurements[12], in blue, and GPS[13], in green. Vertical displacement rates showing subsidence in the Kathmandu basin are not used here, and hence are not shown. Red line is the prediction from the mean model of the posterior Probability Density Function derived using a Bayesian approach. Gray lines show 100 models randomly picked in the posterior PDF. Histograms show the marginals of the slip rate, depth of the tip of the dislocation, dip angle of the dislocation and distance between the tip and the MFT.

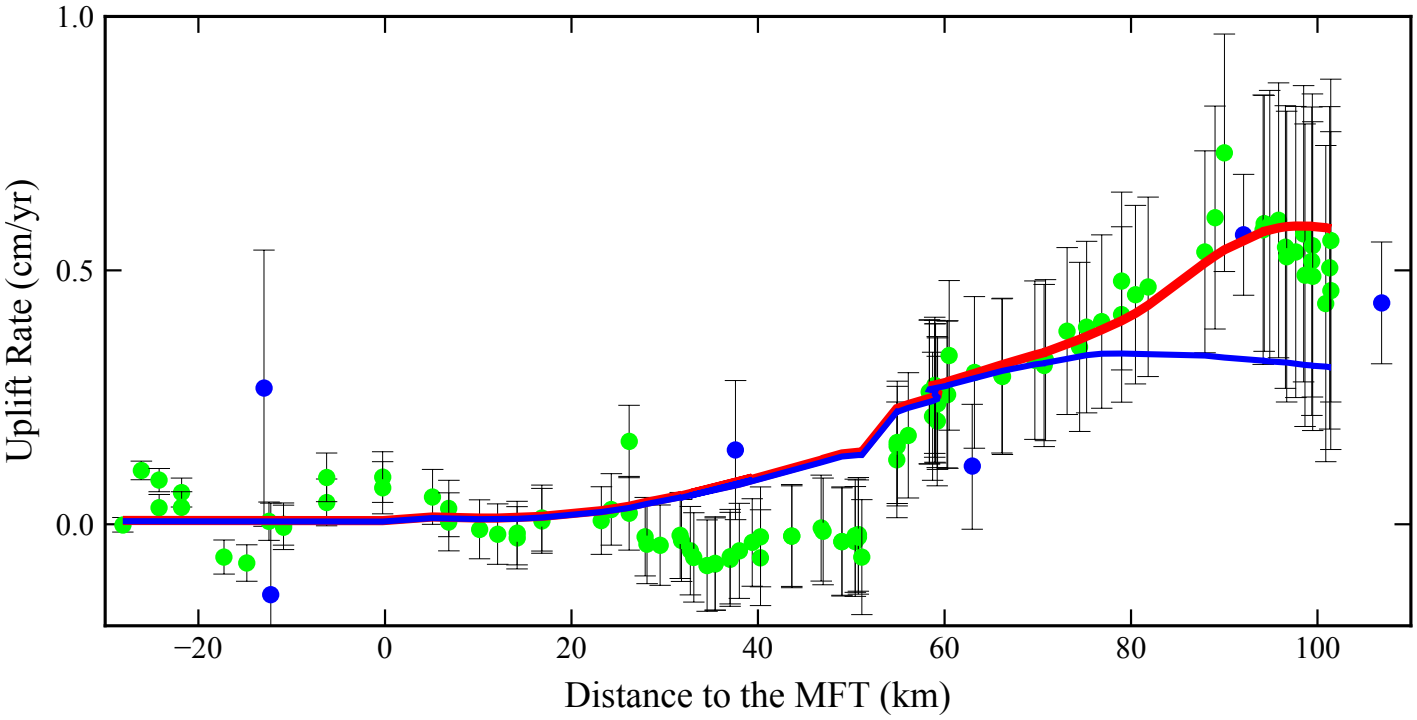

Supplementary Figure 9 | Comparison of the elastic contribution of coupling models to uplift rates. Green dots are the levelling-derived interseismic uplift rates across the Himalaya[12]. Blue dots are GPS-derived uplift rates. Blue line is the vertical displacement rates predicted by the interseismic coupling model from[14], projected onto a flat MHT (i.e. with no steep, mid-crustal, ramp). Red line is the vertical displacement rates predicted by the same interseismic coupling model projected onto our favoured fault geometry, including a steep-mid-crustal ramp. Note that the projection of some deep creep onto the mid-crustal ramp allows to better reproduce the rate of uplift measured at the transition between the Sub-Himalayan and the high chain.

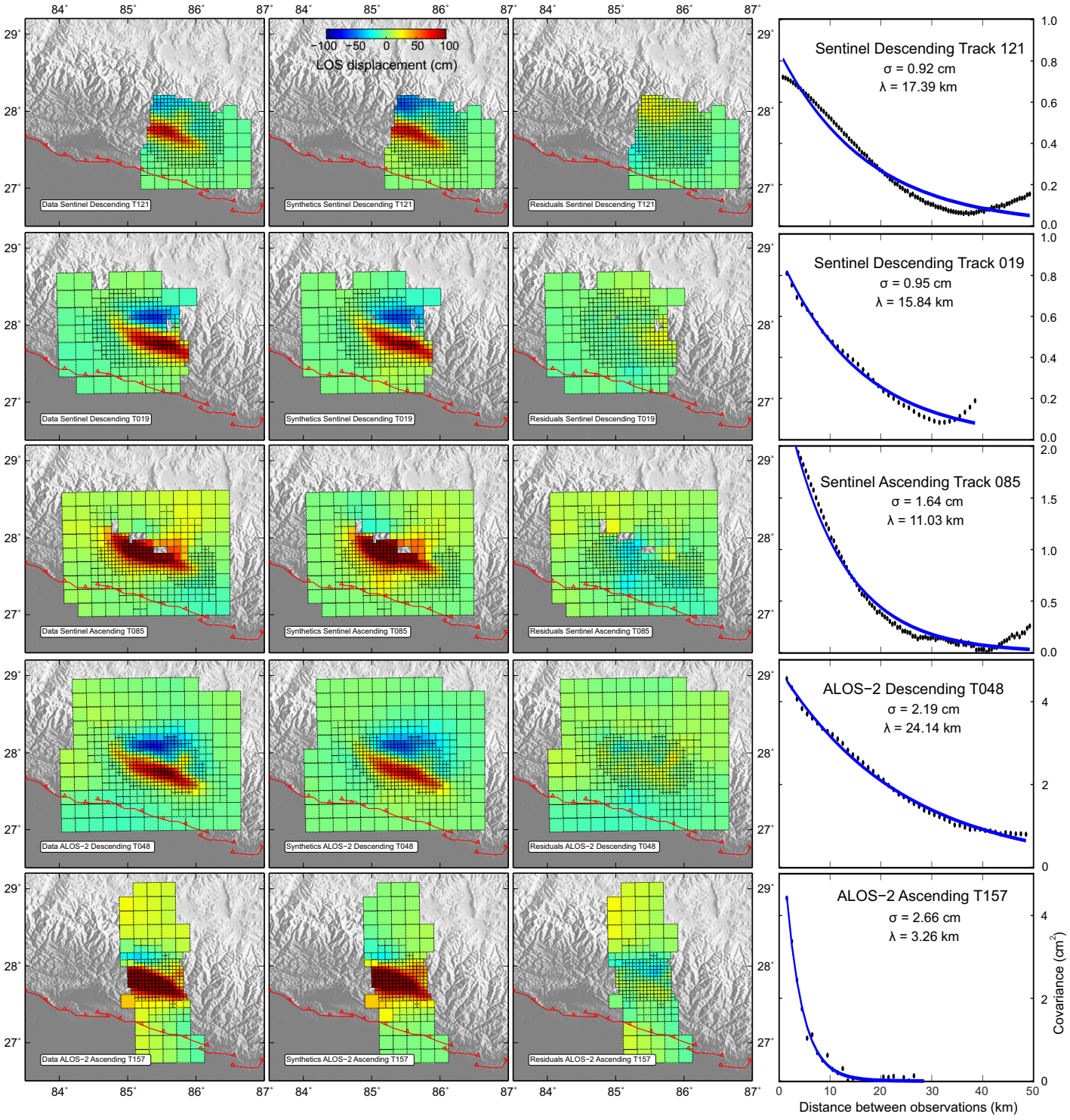

Supplementary Figure 10 | Result of the downsampling procedure on the mainshock coseismic interferograms from Sentinel-1A and ALOS-2, with associated empirical covariance functions. Downsampling scheme used on coseismic interferograms computed from Sentinel-1A acquisitions on track 121 on 24th April and 6th May 2015 (top row), track 19 on 17th and 29th April 2015 (second row) and on track 85 on 9th April and 3rd May 2015 (third row). For ALOS-2 acquisitions on track 48 on 22nd February and 3rd May 2015 (fourth row) and on track 157 on 21st February and 2nd May 2015 (bottom). Each square is a downsampling window over which data are averaged to be used during the slip inversion procedure. Data, predictions from our best model and residuals are shown to the left, center-left and centre-right, respectively. Red line with teeth denotes the surface trace of the Main Frontal Thrust. (right-most column) Empirical covariance function on each interferogram used in the inversion procedure. Black dots show the covariance averaged on the interferogram, over a region where no deformation is observed. Blue line is the best fit exponential decay used to build the data covariance matrix in the inversion procedure.

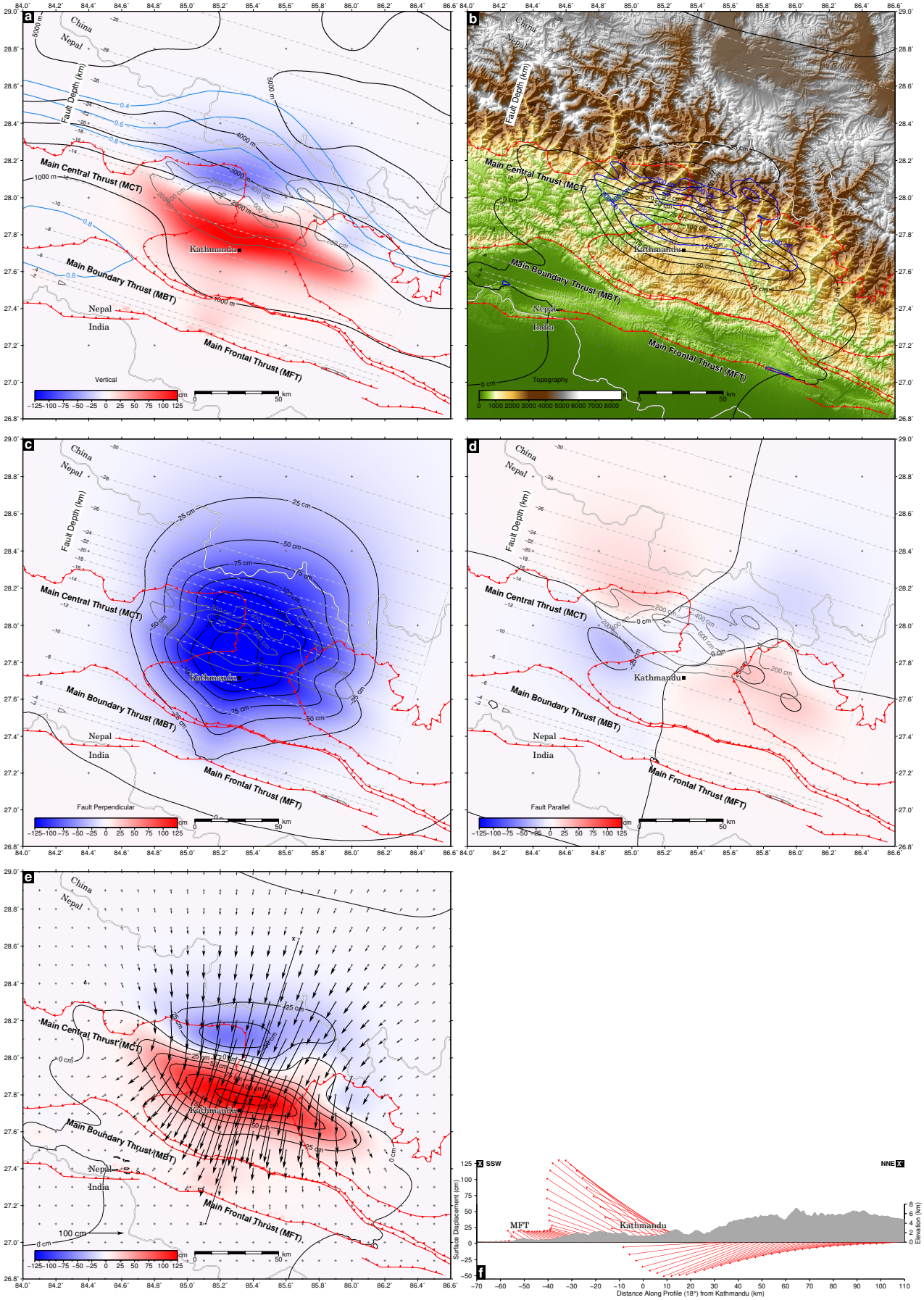

Supplementary Figure 11 | Modelled components of surface displacement due to the mainshock. (a) Modelled vertical motion of the surface with contours of interseismic coupling (blue lines) and smoothed topography (black lines, Gaussian weighted filter, with a 1 sigma of 15 km width). (b) Topography (SRTM3) with contours of modelled vertical displacement overlaid. (c) Modelled fault perpendicular (18°) motion. (d) Modelled fault parallel (108°) motion. (e) Arrows indicate the horizontal motion of the surface at 0.1° intervals based upon the modelled mainshock slip on the MHT. The vertical motion is indicated by the contoured and coloured background. (e) Profile of vertical and fault perpendicular displacements (red arrows) taken along section X–X'.

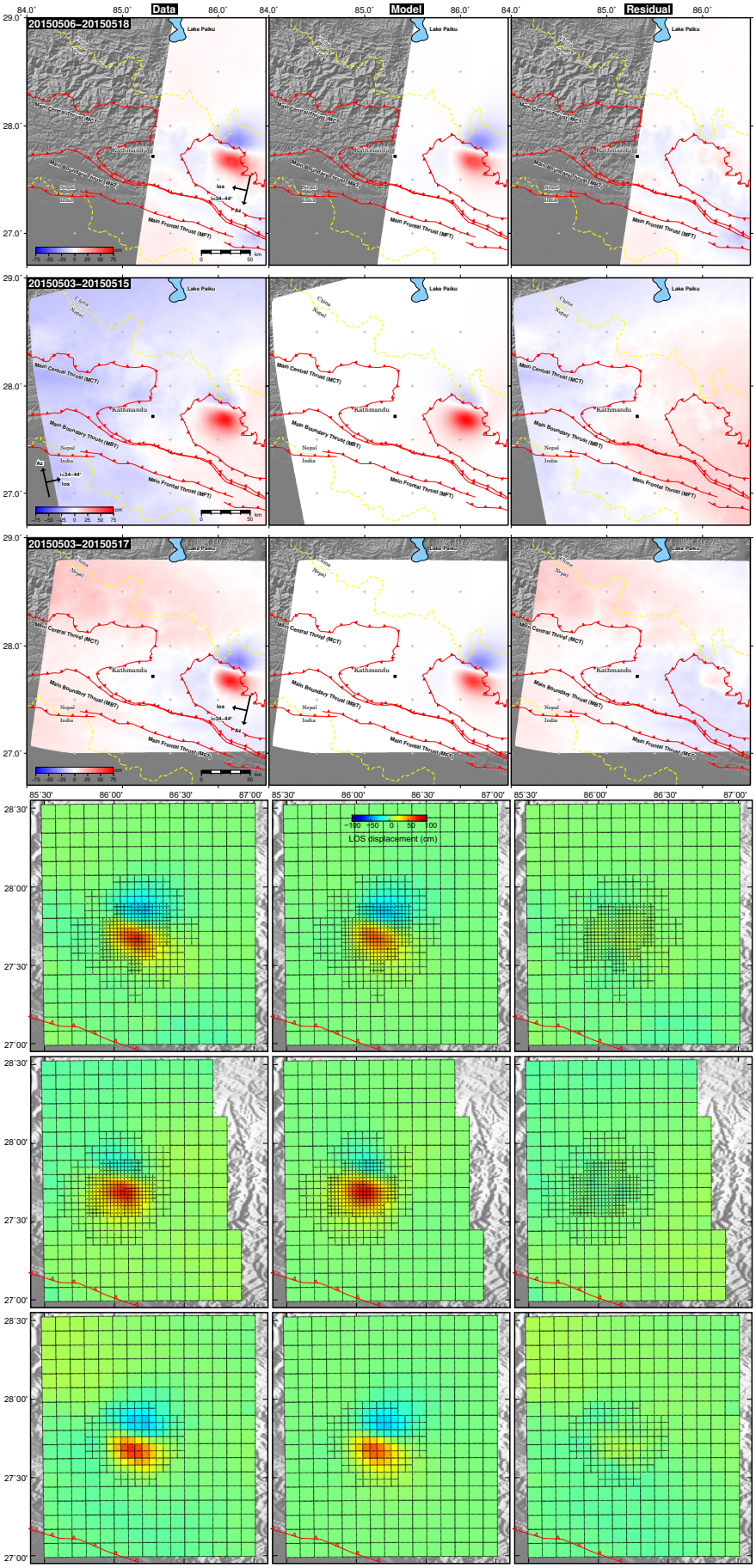

Supplementary Figure 12 | Data, model and residuals for the phase datasets for the Mw 7.1–7.3 aftershock on the 12th April. The fit to the full resolution datasets is shown in the upper three rows. The downsampling scheme used on each of the aftershock coseismic interferograms is shown in the lower three rows. Each square is a downsampling window over which data are averaged to be used during the slip inversion procedure. Data, predictions from our best model and residuals are shown to the left, center and right, respectively. Red lines with teeth are the surface trace of the Main Frontal/Boundary/Central Thrusts (MFT/MBT/MCT).